

Hierarchically Structured LiFePO₄/C with Enhanced Electrochemical Performance for Lithium-Ion Batteries

Xiaojuan Ma, Ligang Gai* and Yan Tian

Institute of Advanced Energy Materials and Chemistry, School of Chemistry and Pharmaceutical Engineering, Qilu University of Technology, Jinan 250353, People's Republic of China

*E-mail: liganggai@qlu.edu.cn

Received: 14 October 2017 / Accepted: 8 December 2017 / Published: 28 December 2017

Carbon-coated LiFePO₄ (LFP/C) has been subjected to extensive research due to its enhanced electronic conductivity, excellent cycling stability, and low cost for application in lithium-ion batteries (LIBs). In this paper, we report on preparation of LFP/C featured with crystalline LFP particles encapsulated into carbon matrix and its electrochemical properties. Hydroxyethyl cellulose (HEC) was employed as an in situ carbon source and structure-directing agent. Controlled anneal treatment of freezing-dried HEC-containing precursor offered the target LFP/C with superior electrochemical performance for LIBs. After 100 cycles at 0.1 and 1 C, the discharge specific capacity of the target sample retains 151.9 and 124.6 mA h g⁻¹, presenting capacity retention of 93.4% and 97.9%, respectively. This result is attributed to crystalline LFP well encapsulated into carbon matrix with enhanced degree of graphitization.

Keywords: LiFePO₄/C; Hydroxyethyl cellulose; Electrochemical performance; Lithium-ion batteries

1. INTRODUCTION

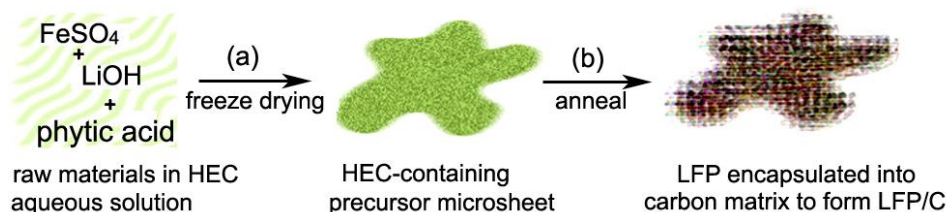
Cathode materials for lithium-ion batteries (LIBs) such as LiCoO₂ [1], LiMn₂O₄ [2], LiMn_xNi_yCo_zO₂ ($x + y + z = 1$) [3], transition metal-based metal-organic frameworks [4], and LiFePO₄ (LFP) [5-28] have been subjected to extensive research due to their crucial roles in determining the energy density, safety, cycle life, and cost of LIBs [5-8]. Compared with the other cathode materials, polyanion-type LFP with olivine structure is a particularly attractive candidate for LIBs, owing to its numerous merits such as a relatively high theoretical capacity (170 mAh g⁻¹), good electrochemical and thermal stability, low cost, environmental compatibility, and a moderate Fe²⁺/Fe³⁺ redox potential at 3.4–3.5 V vs. Li⁺/Li [7, 8]. However, pristine bulk LFP suffers from low electronic conductivity

($\sim 10^{-9}$ S cm $^{-1}$) and slow Li-ion diffusion kinetics ($\sim 10^{-14}$ cm 2 s $^{-1}$) [9, 10]. This limitation hampers its potential application in power LIBs for electric vehicles and hybrid electric vehicles [10].

To address these issues, several strategies have been developed, i.e. reducing the particle size [11], doping with metal/nonmetal elements [7, 9, 12, 23, 27], conjugating with organic/inorganic agents [6, 13, 19, 20], and controlling composition and/or morphology of LFP with surface dominated by (010) plane [8, 14, 15]. In some cases, two or more strategies were combined to offer LFP-based materials with improved electronic conductivity and Li-ion diffusivity and, hence, enhanced electrochemical performance [12, 13, 15, 19, 20, 23]. As demonstrated in literature [15], carbon even poorly crystallized carbon upon the active materials can serve as an effective conduction network for charge transfer. Thus, conjugating LFP with carbon seems to be the most promising technique to produce cathode materials with superior electrochemical performance [5]. In LFP/C composites, the carbon component can be easily formed by in situ pyrolysis of organic carbon precursors such as glucose [16, 25], fructose [9], starch [12], sucrose [17], Tween [18], citrate [8, 17, 21], polymethyl methacrylate [26], polyethylene glycol [16, 17], polyvinylpyrrolidone [7], polyaniline [19], polypyrrole [20], HEC [21], triblock copolymer [6], and β -cyclodextrin [16]. The carbon sources have important effects on structure, morphology, particle size, and specific surface area of the composite electrode materials [16-18]. As a result, LFP/C composites with superior electrochemical performance can be produced by selecting appropriate organic carbon precursors.

Cellulose is an eco-friendly biopolymer with abundance in nature. As one of cellulose derivatives, hydroxyethyl cellulose (HEC) (Fig. S1) has been widely used in drug delivery [29], polymer light-emitting diodes [30], sensors [31], skin tissue engineering [32], and desulfurization of gasoline [33]. However, there are few reports on using HEC as the in situ carbon source and structure-directing agent for synthesis of electrode materials [21].

In this paper, we report on fabrication of LFP/C featured with crystalline LFP encapsulated into carbon matrix through controlled anneal treatment of freeze-dried HEC-containing precursor and their electrochemical performance for LIBs. The synthetic strategy is based on: (1) freeze drying presents a simple approach to obtain uniformly distributed template-containing precursors in which components of the target materials were mixed at atomic level [3, 24, 26, 34]; (2) freeze drying of HEC solution results in formation of HEC microsheets (Fig. S2a), which serve as a structure-directing agent to form precursor counterparts of the target product (Scheme 1a and Fig. S2b); and (3) anneal treatment of the precursor counterparts in reducing atmosphere produces the target product (Scheme 1b and Fig. S2c). The target LFP/C exhibits superior or comparable electrochemical performance at low current rates as compared with LFP/C composites in previous reports [6, 7, 13, 20, 27, 28].



Scheme 1. Illustration of formation of LFP/C.

2. EXPERIMENTAL

2.1. Synthesis of LFP/C

LFP/C was derived from annealing HEC-containing precursor counterpart, which was obtained by freeze drying of HEC solution containing the components of the target material. In brief, 0.15 g of HEC was dissolved into 60 mL of distilled water at 45 °C with Ar bubbling, followed by addition of 3 mmol $\text{FeSO}_4 \cdot 7\text{H}_2\text{O}$, 3 mmol $\text{LiOH} \cdot \text{H}_2\text{O}$, and 3 mmol phytic acid. The mixture was stirred at room temperature for 2 h, allowed to cool to minus 18 °C in an ice-box, and then freeze-dried to form fluffy powders. LFP/C was obtained by annealing the fluffy powders in N_2/H_2 (95:5, v/v) at 700, 750, and 780 °C for 8 h, respectively, with a ramping rate of 5 °C min^{-1} . The LFP/C samples are named LFP/C- T , where T denotes the anneal temperature.

2.2. Characterization

X-ray powder diffraction (XRD) patterns were recorded on a Bruker D8 Advance diffractometer with Cu $K\alpha$ radiation, operating at 40 kV and 40 mA. Raman spectra were collected at room temperature on a Horiba Jobin Yvon laser confocal micro-Raman spectrometer with a 532 nm yttrium aluminum garnet laser. Scanning electron microscopy (SEM) images were taken on a Hitachi S-4800 field-emission scanning electron microscope. Transmission electron microscopy (TEM) images were taken on a JEOL JEM-2100 high-resolution transmission electron microscope, operating at an accelerating voltage of 200 kV. Thermogravimetric (TG) and differential scanning calorimetric (DSC) analysis were carried out on a Perkin-Elmer DSC-2C thermogravimetric analyzer, operating at a heating rate of 10 °C min^{-1} in air.

Nitrogen sorption isotherms were collected at 77.3 K using a Micromeritics TriStar II 3020 sorption analyzer. The Brunauer–Emmett–Teller (BET) method was utilized to calculate the specific surface areas (S_{BET}). Pore size distribution (PSD) plots were derived from adsorption data through the Barrett–Joyner–Halenda (BJH) method. Before recording the nitrogen sorption isotherms, the samples were degassed at 200 °C for 6 h.

2.3. Electrochemical tests

Electrochemical properties of the samples were evaluated in terms of cyclic voltammograms (CVs), galvanostatic charge/discharge (GCD), electrochemical impedance spectroscopy (EIS), rate capability, and cycling stability, by assembling CR2032 coin cells in configuration of Li metal(–)|electrolyte|LFP/C(+) with organic electrolyte, using microporous polypropylene film (Celgard 2400) as the separator. The electrolyte was 1 mol L^{-1} LiPF_6 dissolved in ethylene carbonate/dimethyl carbonate/diethyl carbonate (1:1:1, v/v) mixed solution (MTI Kejing Group, Hefei, China). The positive electrode was prepared by blade-coating homogeneously blended slurry onto an aluminum foil, and then dried in a vacuum oven at 80 °C for 12 h. The slurry was composed of 70 wt% active material, 20 wt% acetylene black, and 10 wt% polyvinylidene fluoride in *N*-methylpyrrolidone. The

aluminum foil with coating was double-rolled and then cut into circular sheets with diameter of 12 mm. The mass of active material in a cell was in the range of 2–3 mg. Cell assembly was conducted in an Ar-filled glove box, where oxygen and moisture were kept below 5 ppm.

CVs were recorded on a CHI 660E electrochemical workstation (Shanghai CH Instruments Co., China). The applied potential was in the range of 2.5–4.2 V for LFP/C vs. Li^+/Li . GCD curves of the coin cells were collected on a LANHE CT2001A battery tester (Wuhan Landian Co., China), at current rates ranging from 0.1 to 5 C. In view of the small capacitive contribution of carbon in the potential range of 2.5–4.2 V, the specific capacity of LFP/C was calculated by excluding the contribution of the carbon component [7]. Alternating current (AC) EIS spectra were recorded on the CHI 660E electrochemical workstation with AC amplitude of 5 mV, at a frequency range of 10^{-2} – 10^5 Hz.

3. RESULTS AND DISCUSSION

3.1 Structure, composition, and morphology

Fig. 1 shows the XRD spectra of LFP/C samples. The diffraction peaks in LFP/C-700 (Fig. 1a) and LFP/C-750 (Fig. 1b) spectra agree well with those of orthorhombic LFP with space group of Pnma (62) (JCPDS 81-1173), indicating formation of pure phase of LFP. In LFP/C-780 spectrum (Fig. 1c), however, hexagonal Fe_2P with space group of P321 (150) (JCPDS 27-1171) occurs, apart from LFP. The appearance of Fe_2P is due to self-redox reaction of LFP annealed at elevated temperatures. Previous report showed Fe_2P occurred at 840 °C for LFP/C precursors annealed in Ar [17]. In the present case, the appearance of Fe_2P at 780 °C indicates that the reducing atmosphere (N_2/H_2 , 95:5, v/v) promotes decomposition of LFP, consistent with the previous report [35]. The role of iron phosphides (Fe_2P , Fe_3P) in electrochemical performance of LFP depends on whether their concentration is above a critical value [17, 35].

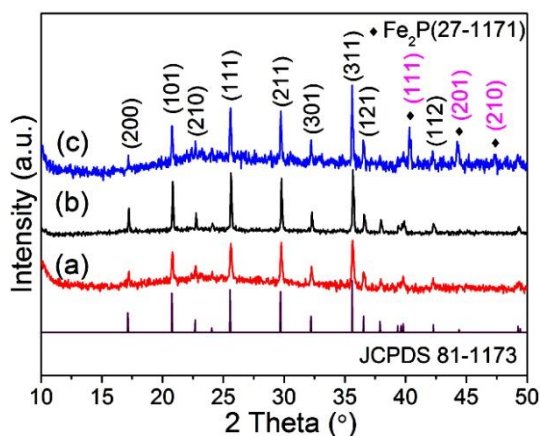


Figure 1. XRD spectra of the samples: (a) LFP/C-700; (b) LFP/C-750; (c) LFP/C-780.

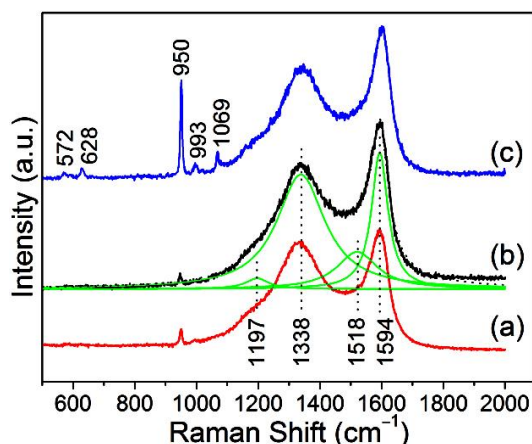


Figure 2. Raman spectra of the samples: (a) LFP/C-700; (b) LFP/C-750; (c) LFP/C-780.

To further reveal the composition of LFP/C samples, Raman spectra were collected as shown in Fig. 2. Five bands around 572, 628, 950, 993, and 1069 cm^{-1} belonging to LFP occur in LFP/C-780 spectrum (Fig. 2c) [14, 36]. The former two bands and the latter three bands correspond separately to the bending modes (ν_4) and the stretching modes (ν_1 and ν_3) of PO_4 tetrahedron in LFP [14, 36]. However, only one small band at 950 cm^{-1} , corresponding to PO_4 symmetrically stretching vibrations of LFP, can be observed in LFP/C-700 (Fig. 2a) and LFP/C-750 spectra (Fig. 2b) [18]. This result indicates that LFP component is nearly encapsulated into the carbon matrix [19]. The carbon component is reflected by the intense bands centered at 1338 and 1594 cm^{-1} , which can be assigned separately to the D (disordered) and G (graphitic) bands of Raman vibration modes for carbon [18, 19]. The D and G bands can be deconvolved into four components through Lorentzian functions (Table S1) [37]. Taking LFP/C-750 spectrum as an example, four components centered at 1197 (D4), 1338 (D1), 1518 (D3), and 1594 cm^{-1} (G) can be resolved (Fig. 2b, green lines). The bands at 1338 and 1594 cm^{-1} are related to sp^2 graphitic carbon while the other bands are associated with sp^3 -type carbon [18]. The intensity ratio of I_D/I_G is a signal of the degree of graphitization in partially graphitic carbons. A lower I_D/I_G ratio indicates a higher degree of graphitization and, hence, an improved electronic conductivity [18, 19]. In the present case, the I_{D1}/I_G ratios for LFP/C-750 and LFP/C-780 are lower than that for LFP/C-700 (Table 1). This result implies the former two samples serving as electrode materials favor electron transfer.

Table 1. Physicochemical properties of the samples.

sample	S_{BET} ($\text{m}^2 \text{g}^{-1}$)	total pore volume ($\text{cm}^3 \text{g}^{-1}$)	average pore diameter (nm)	I_{D1}/I_G
LFP/C-700	43.9	0.19	17.5	1.01
LFP/C-750	47.5	0.18	14.9	0.84
LFP/C-780	86.6	0.18	10.4	0.83

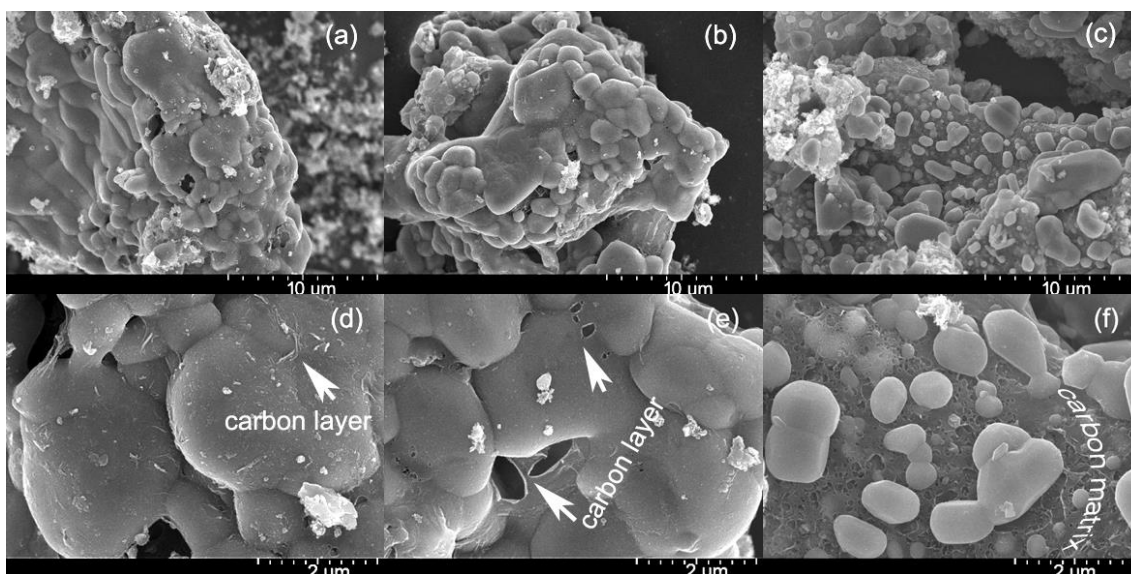


Figure 3. SEM images of LFP/C samples: (a,d) LFP/C-700; (b,e) LFP/C-750; (c,f) LFP/C-780.

Fig. 3 shows the field-emission SEM images of LFP/C samples. The samples are mainly composed of aggregated microparticles, which are constructed by LFP particles protruding above (Fig. 3c,f) or encapsulated into carbon matrix (Fig. 3a,b,d,e). With respect to LFP/C-700 (Fig. 3d) and LFP/C-750 (Fig. 3e), the LFP particles are coated by carbon layers. However, many LFP particles protrude above the carbon matrix for LFP/C-780 (Fig. 3f). This result indicates that anneal treatment at 780 °C facilitates growth and coarsening of LFP particles so that they break through the carbon coating. As documented in literature [38], complete coating of carbon upon LFP favors charge transfer and, hence, plays a crucial role in achieving good electrochemical performance.

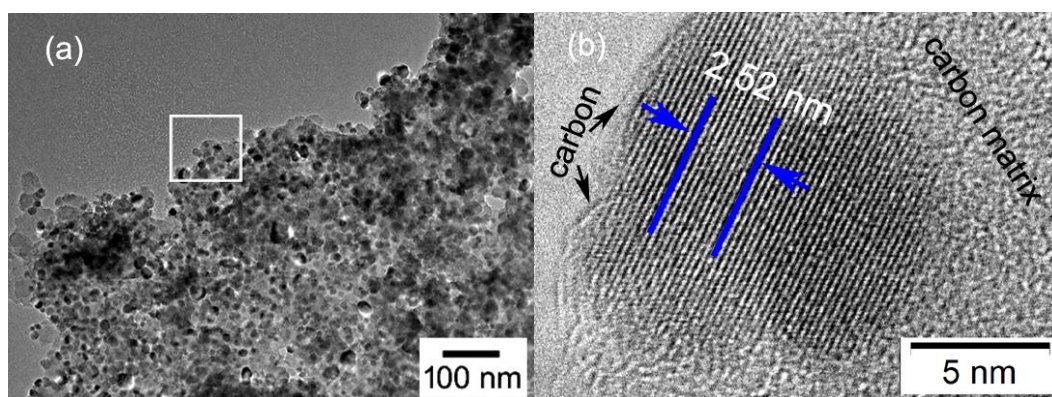


Figure 4. TEM images of LFP/C-750: (a) low magnification; (b) high-resolution image corresponding to the squared area in a.

The nanoparticles encapsulated into carbon matrix for LFP/C-750 can be clearly observed from the TEM images (Fig. 4). The size of LFP nanoparticles is in the range of 10–20 nm. Lattice fringes with d -spacing of 0.252 nm correspond to the (311) plane of LFP (Fig. 4b). This result indicates LFP/C

microparticles are constituted by LFP nanoparticles embedded in turbostratic carbon matrix, presenting a hierarchical structure. Hierarchical structures possess relatively high surface area and copious active sites for reaction on the surface, a situation that is beneficial for providing superior electrochemical performance [35].

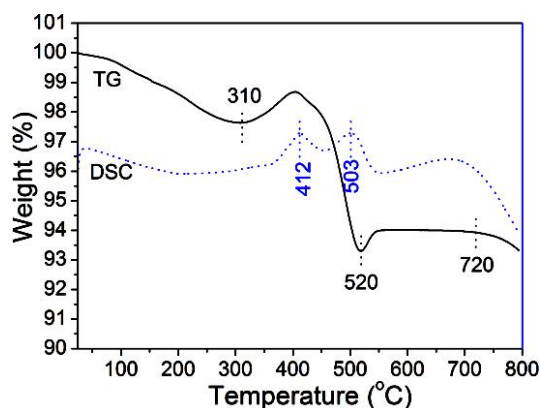
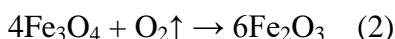


Figure 5. TG/DSC curves of LFP/C-750.

The mass percentage of carbon component was determined by the TG/DSC analysis. Taking LFP/C-750 as an example (Fig. 5), the monotonously descending TG curve from room temperature to 200 °C is due to removal of surface-adsorbed water [6]. This situation is reflected by a broad endothermic peak centered at 200 °C in DSC curve. The decline of the TG curve continues at the temperature ranging from 200 to 310 °C, due to onset burning of the carbon component. However, an abnormal rise in TG curve occurs from 310 to 402 °C. The reason is that the burning of carbon is overwhelmed by redox reaction of LFP with O₂ (eq 1) [34], providing a theoretical weight gain of 5.06%. The phase transformation of LFP is reflected by an exothermic peak centered at 412 °C in DSC curve. The dramatic drop in TG curve at the temperature range of 402–520 °C is assigned to complete removal of the carbon component. This stage corresponds to an exothermic peak centered at 503 °C in DSC curve. The small rise in TG curve at the temperature above 520 °C is attributed to phase transformation to Fe₂O₃ from Fe₃O₄ (eq 2) [39]. The slow decline in TG curve at the temperature above 720 °C is related to evaporation of lithium oxide from LFP [6]. By incorporation of the theoretical weight gain of 5.06% according to eq (1), the weight percentage of LFP/C-700, LFP/C-750, and LFP/C-780 can be calculated to be 13.1%, 10.5%, and 9.9%, respectively.



3.2 Textural properties

The textural properties of LFP/C samples were revealed by the N₂ sorption isotherms and the PSD plots (Fig. 6). The isotherms (Fig. 6a) exhibit type-IV adsorption/desorption with type-H3 hysteresis loop according to BDDT classification [40]. The hysteresis loops occurring at a relative

pressure range of 0.4–1.0 reveal coexistence of mesopores (2–50 nm) and macropores (> 50 nm) [41], as shown by the PSD plots (Fig. 6b). The S_{BET} and pore characteristics are listed in Table 1. The relatively larger S_{BET} for LFP/C-780 is due to the particles protruding out of the carbon matrix (Fig. 3f). The mesopores and macropores not only favor electrolyte diffusion to active sites with less resistance, but also tolerate the volume change of active materials during charge/discharge cycles [41].

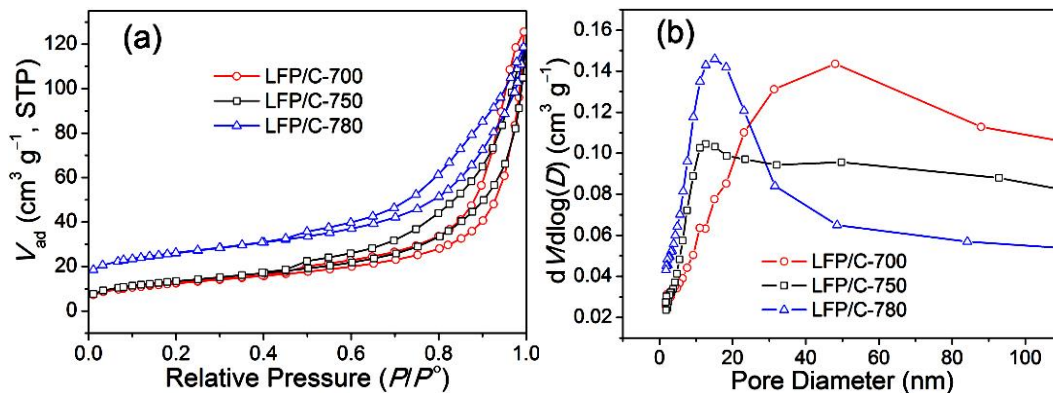
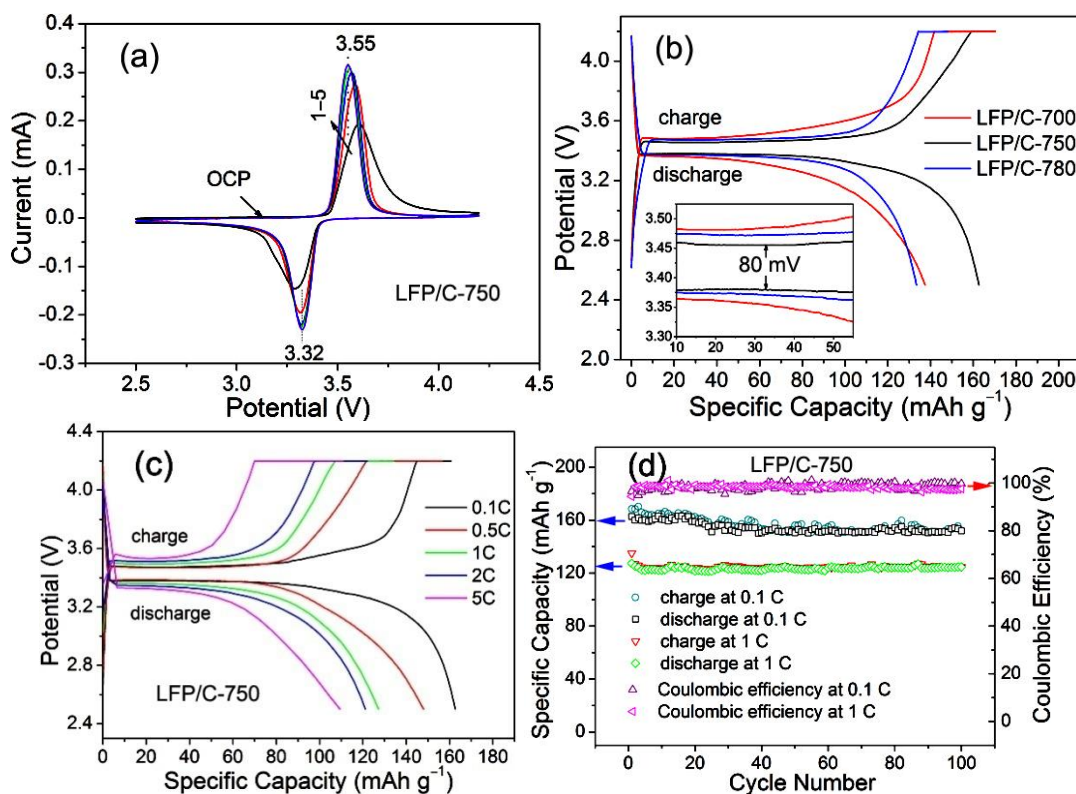


Figure 6. (a) N_2 sorption isotherms; (b) PSD plots.

On the basis of the above analysis, LFP/C samples have been produced by annealing HEC-containing precursors obtained through a freeze-drying method.



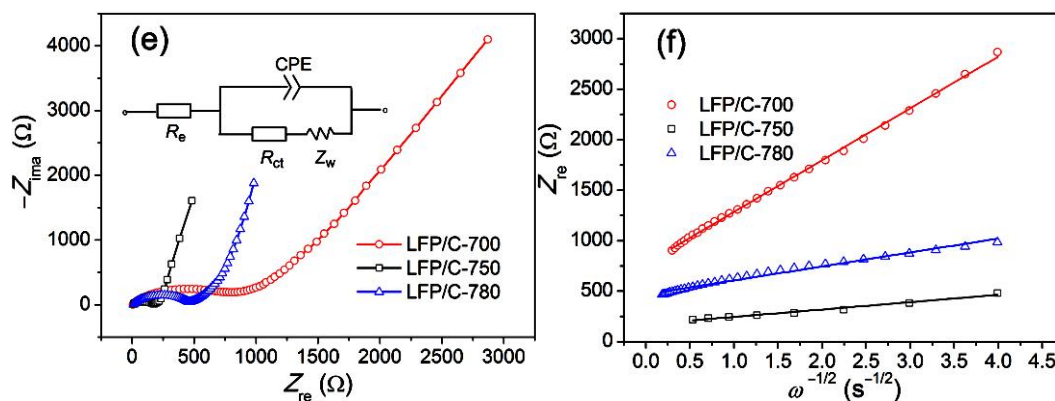


Figure 7. (a) CVs of LFP/C-750; (b) GCD curves of LFP/C samples at 0.1 C; (c) rate capability of LFP/C-750; (d) cycling performance of LFP/C-750 at 0.1 and 1 C; (e) Nyquist plots; (f) plots of Z_{re} versus $\omega^{-1/2}$.

The anneal temperature plays crucial roles in determining physicochemical properties of the composites. Among the samples, LFP/C-750 possesses moderate carbon concentration, S_{BET} , and pore diameter. Also, LFP/C-750 exhibits improved graphitization degree of carbon component compared with LFP/C-700, while presents pure phase of LFP and better carbon coating in comparison with LFP/C-780. These physicochemical properties of LFP/C-750 ensure its superior electrochemical performance for LIBs.

3.3 Electrochemical tests

Fig. 7a shows the CVs of LFP/C-750 with a scan rate of 0.1 mV s^{-1} in a potential range of 2.5–4.2 V. An anodic peak and a cathodic peak with good symmetry are observed and stabilize at 3.55 and 3.32 V after three cycles. This indicates good stability of lithium insertion/extraction in LFP/C-750 [8]. The potential gap between the redox peaks is ca. 0.23 V, lower than that of ca. 0.26 V for LFP/C-780 (Fig. S3a) and that of 0.5 V for LFP/C-700 (Fig. S3b). This result indicates superior electrode kinetics and electrochemical reversibility of LFP/C-750 [10]. As mentioned before, the role of Fe_2P in electrochemical performance of LFP depends on its concentration [17, 35]. Considering that we cannot determine the concentration of Fe_2P in LFP/C-780, it is not necessary to correlate the electrochemical performance of LFP/C-780 with Fe_2P .

Fig. 7b presents the GCD curves of LFP/C recorded at 0.1 C. A flat discharge potential plateau is observed at ca. 3.4 V for all LFP/C samples, indicating a two-phase redox reaction through a first-order transition between LFP and FePO_4 [6, 26]. The discharge specific capacity (C_{dis}) of LFP/C-750 is $162.7 \text{ mA h g}^{-1}$, higher than that of $137.5 \text{ mA h g}^{-1}$ for LFP/C-700 and that of $133.5 \text{ mA h g}^{-1}$ for LFP/C-780. The superior electrochemical performance of LFP/C-750 is also reflected by a smaller charge/discharge plateau interval of 80 mV, compared with that of 100 mV for LFP/C-700 and that of 130 mV for LFP/C-780 (Fig. 7b, inset). This result indicates lower electrode polarization and better reaction kinetics of LFP/C-750 [6, 26], in concert with the CV result. The superior electrochemical

performance of LFP/C-750 is attributed to its enhanced degree of carbon graphitization compared with LFP/C-700 and to higher phase purity and better carbon coating compared with LFP/C-780.

In view of the superior electrochemical performance of LFP/C-750, further electrochemical tests were performed on LFP/C-750. With increasing the charge/discharge rate from 0.1 to 0.5, 1, 2, and 5 C, the C_{dis} of LFP/C-750 decreases from 162.7 to 148.0, 127.3, 122.0, and 109.4 mA h g⁻¹, respectively (Fig. 7c). After 100 cycles at 0.1 and 1 C, LFP/C-750 exhibits capacity retention of 93.4% and 97.9% relative to the initial values at 0.1 (162.7 mA h g⁻¹) and 1 C (127.3 mA h g⁻¹), respectively (Fig. 7d). The Coulombic efficiency approaches to 100% during the cycling process (Fig. 7d), indicating good electrochemical reversibility of LFP/C-750. The cycling performance of LFP/C-750 presented here is superior or comparable to that of LFP/C in previous reports (Table 2).

Table 2. Comparison of electrochemical performance of LFP/C at room temperature.

sample	rate/cycle number	retained C_{dis} (mA h g ⁻¹)	rate/cycle number	retained C_{dis} (mA h g ⁻¹)	ref.
LFP/C nanostructures	0.1 C/100	151	1 C/100	–	[6]
LFP/C nanofibers	0.1 C/100	124	1 C/100	–	[7]
LFP/C-BTFSI	0.1 C/100	91*	1 C/100	–	[13]
LFP/C/PPy	0.1 C/100	–	1 C/100	100	[20]
LFP/C microspheres	0.1 C/100	–	1 C/100	120	[27]
Ti-doped LFP/C	0.1 C/30	134.7	1 C/100	–	[28]
LFP/C microparticles	0.1 C/100	151.9	1 C/100	124.6	this work

*Values estimated from the information given in literature.

To reveal the reaction kinetics of LFP/C samples, EIS spectra were collected as shown in Fig. 7e. The intercepts on the realistic axis at the high frequency end represent the equivalent series resistance (ESR), which consists of the bulk electrolyte resistance, internal resistance of active materials, and interfacial resistance between the active materials and current collector [42]. The depressed semicircles in the high-middle frequency region correspond to the charge transfer resistance (R_{ct}). The inclined lines in the low frequency region represent the Warburg impedance (Z_{w}) associated with Li⁺ diffusion in the bulk of the electrode [10, 13]. Although the ESR for LFP/C-700, is smaller than that for LFP/C-750, the R_{ct} value for LFP/C-750 is much smaller than that for LFP/700 and LFP/C-780 (Table 3). Also, the inclined line of LFP/C-750 approaches nearer to the imaginary axis compared with those of LFP/C-700 and LFP/C-780. These results indicate improved charge transfer and redox reaction kinetics for LFP/C-750 [10], in concert with the CV and GCD results. The Nyquist plots can be well fitted by an equivalent circuit as shown in Fig. 7e (inset). The Li⁺ diffusion

coefficient (D_{Li}) can be calculated from the data of inclined lines in Nyquist plots according to eq (3) [10]:

$$D_{\text{Li}} = R^2 T^2 / 2 A^2 n^4 F^4 C^2 \sigma_w^2 \quad (3)$$

where R is the gas constant ($8.314 \text{ J mol}^{-1} \text{ K}^{-1}$), T the absolute temperature (298.15 K), A the surface area of the electrode (cm^2), n the number of transferred electrons per LFP during the electrochemical reaction ($n = 1$), F the Faraday constant ($96,485 \text{ C mol}^{-1}$), C the molar concentration of Li^+ in LFP, and σ_w the Warburg coefficient associated with Z_{re} , i.e. $Z_{\text{re}} \propto \sigma_w \omega^{-1/2}$ [16]. Therefore, σ_w can be obtained by linearly fitting the plot of Z_{re} versus $\omega^{-1/2}$ (Fig. 7f), where ω equals to $2\pi f$ with f being in the low frequency region. The σ_w and D_{Li} values are provided in Table 3. The D_{Li} for LFP/C-750 is higher than that for LFP/C-780 and LFP/C-700. This result confirms that complete carbon coating with improved degree of graphitization facilitates to improve the diffusion of Li^+ during charge/discharge cycles.

Table 3. Impedance parameters of the samples.

sample	ESR (Ω)	R_{ct} (Ω)	σ_w ($\Omega \text{ cm}^2 \text{ s}^{-1/2}$)	D_{Li} ($\text{cm}^2 \text{ s}^{-1}$)
LFP/C-700	6.2	874.9	512.8	3.25×10^{-15}
LFP/C-750	11.0	194.1	73.3	1.59×10^{-13}
LFP/C-780	10.2	443.6	138.0	4.48×10^{-14}

4. CONCLUSION

In summary, LFP/C sample with LFP encapsulated into carbon matrix has been prepared by freeze drying of HEC-containing precursor post anneal treatment. The scientific significance of this research is: (1) LFP/C with crystalline LFP particles encapsulated into carbon matrix exhibits superior electrochemical performance as compared to LFP/C with LFP particles protruding on carbon matrix; and (2) the abundance of eco-friendly HEC and phytic acid provide alternative carbon and phosphorous sources for synthesis of polyanion-type electrode materials.

ACKNOWLEDGEMENT

This work was financially supported by Natural Science Foundation of China under Grant No. 51272143.

SUPPORTING MATERIAL

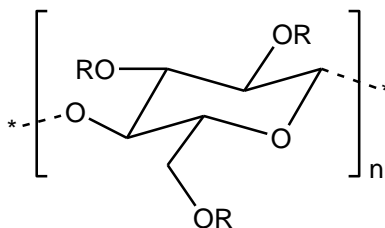


Figure S1 Molecular structure of HEC, where R denotes H or $\text{CH}_2\text{CH}_2\text{OH}$.

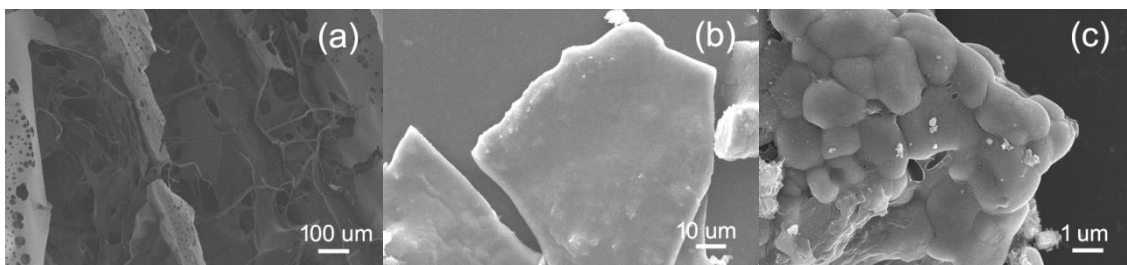


Fig. S2 SEM images of: (a) HEC microsheets; (b) HEC-containing precursor microparticles; (c) LFP/C.

Table S1. Results of Lorentzian fittings of the Raman spectra.

Sample	peak position (cm^{-1})				$I_{\text{D1}}/I_{\text{G}}$
	D4	D1	D3	G	
$\text{LiFePO}_4/\text{C}-700$	1184	1335	1523	1594	1.01
$\text{LiFePO}_4/\text{C}-750$	1197	1338	1518	1594	0.84
$\text{LiFePO}_4/\text{C}-780$	1183	1342	1527	1601	0.83

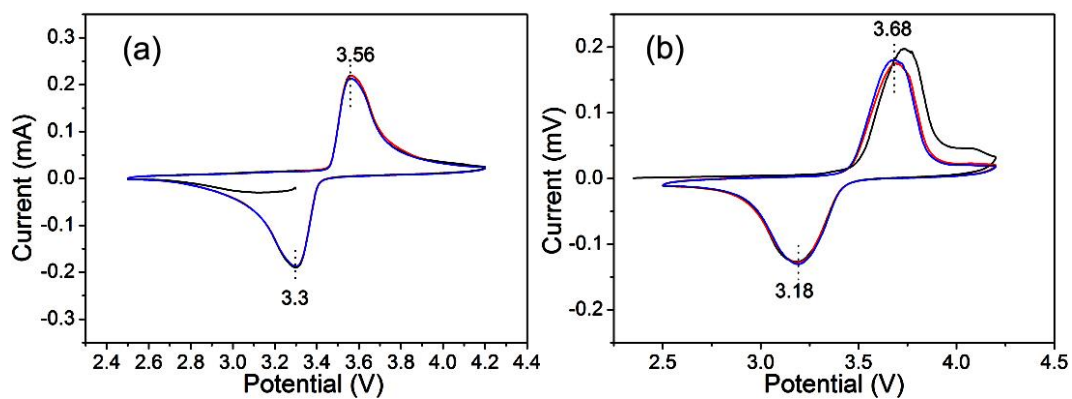


Fig. S3 (a) CVs of LFP/C-780; (b) LFP/C-700.

References

1. Zhou, Y. Lu, Q. Wang, J. Xu, W. Wang, X. Dai and J. Li, *J. Power Sources* 346 (2017) 24.
2. C.-G. Han, C. Zhu, G. Saito, N. Sheng, T. Nomura and T. Akiyama, *Electrochim. Acta* 224 (2017) 71.
3. S.J. Shi, J.P. Tu, Y.Y. Tang, Y.X. Yu, Y.Q. Zhang and X.L. Wang, *J. Power Sources* 221 (2013) 300.
4. S. Zheng, X. Li, B. Yan, Q. Hu, Y. Xu, X. Xiao, H. Xue and H. Pang, *Adv. Energy Mater.* 7 (2017) 1602733.
5. A. Eftekhari, *J. Power Sources* 343 (2017) 395.
6. L. Bao, L. Li, G. Xu, J. Wang, R. Zhao, G. Shen, G. Han and S. Zhou, *Electrochim. Acta* 222 (2016) 685.
7. Y.C. Lee, D.W. Han, M. Park, M.R. Jo, S.H. Kang, J.K. Lee and Y.M. Kang, *ACS Appl. Mater. Interfaces* 6 (2014) 9435.
8. S. Li, X. Liu, R. Mi, H. Liu, Y. Li, W.M. Lau and J. Mei, *ACS Appl. Mater. Interfaces* 6 (2014) 9449.
9. I.D. Johnson, M. Lübke, O.Y. Wu, N.M. Makwana, G.J. Smales, H.U. Islam, R.Y. Dedigama, R.I. Gruar, C.J. Tighe, D.O. Scanlon, F. Corà, D.J.L. Brett, P.R. Shearing and J.A. Darr, *J. Power Sources* 302 (2016) 410.
10. X. Tian, Y. Zhou, X. Tu, Z. Zhang and G. Du, *J. Power Sources* 340 (2017) 40.
11. P. Gibot, M. Casas-Cabanas, L. Laffont, S. Levasseur, P. Carlach, S. Hamelet, J.M. Tarascon and C. Masquelier, *Nat. Mater.* 7 (2008) 741.
12. J.-W. Zhao, S.-X. Zhao, X. Wu, H.-M. Cheng and C.-W. Nan, *J. Alloys Compd.* 699 (2017) 849.
13. N. Delaporte, A. Perea, E. Lebegue, S. Ladouceur, K. Zaghbi and D. Belanger, *ACS Appl. Mater. Interfaces* 7 (2015) 18519.
14. Y. Zhao, L. Peng, B. Liu and G. Yu, *Nano Lett.* 14 (2014) 2849.
15. B. Kang and G. Ceder, *Nature* 458 (2009) 190.
16. X. Yang, J. Tu, M. Lei, Z. Zuo, B. Wu and H. Zhou, *Electrochim. Acta* 193 (2016) 206.
17. F. Yu, J. Zhang, Y. Yang and G. Song, *Electrochim. Acta* 54 (2009) 7389.
18. Q. Li, F. Zheng, Y. Huang, X. Zhang, Q. Wu, D. Fu, J. Zhang, J. Yin and H. Wang, *J. Mater. Chem. A* 3 (2015) 2025.
19. H. Wang, L. Liu, R. Wang, D. Zhang, L. Zhu, S. Qiu, Y. Wei, X. Jin and Z. Zhang, *J. Mater. Chem. A* 3 (2015) 8062.
20. I. Boyano, J.A. Blazquez, I. de Meatza, M. Bengoechea, O. Miguel, H. Grande, Y. Huang and J.B. Goodenough, *J. Power Sources* 195 (2010) 5351.
21. R. Dominko, M. Bele, M. Gaberscek, M. Remskar, D. Hanzel, S. Pejovnik and J. Jamnik, *J. Electrochem. Soc.* 152 (2005) A607.
22. H. Shu, M. Chen, Y. Fu, X. Yang, X. Yi, Y. Bai, Q. Liang, Q. Wei, B. Hu, J. Tan, C. Wu, M. Zhou and X. Wang, *J. Power Sources* 252 (2014) 73.
23. H. Shu, X. Wang, Q. Wu, B. Hu, X. Yang, Q. Wei, Q. Liang, Y. Bai, M. Zhou, C. Wu, M. Chen, A. Wang and L. Jiang, *J. Power Sources* 237 (2013) 149.
24. V. Palomares, A. Goñi, I.G.d. Muro, I. de Meatza, M. Bengoechea, O. Miguel and T. Rojo, *J. Power Sources* 171 (2007) 879.
25. N. Zhao, Y. Li, X. Zhao, X. Zhi and G. Liang, *J. Alloys Compd.* 683 (2016) 123.
26. X. Tian, Y. Zhou, G. Wu, P. Wang and J. Chen, *Electrochim. Acta* 229 (2017) 316.
27. C.-l. Fan, C.-r. Lin, S.-c. Han, J. Chen, L.-f. Li, Y.-m. Bai, K.-h. Zhang and X. Zhang, *New J. Chem.* 38 (2014) 795.
28. J. Su, X.-L. Wu, C.-P. Yang, J.-S. Lee, J. Kim and Y.-G. Guo, *J. Phys. Chem. C* 116 (2012) 5019.
29. B.J. Kong, A. Kim and S.N. Park, *Carbohydr. Polym.* 147 (2016) 473.
30. C.-L. Wu and Y. Chen, *Org. Electron.* 25 (2015) 156.
31. M.Z. Muhammad, A. Lokman, M. Batumalay, H. Arof, H. Ahmad and S.W. Harun, *Adv. Mater. Sci.*

- Eng. 2013 (2013) 1.
32. F.H. Zulkifli, F.S. Hussain, M.S. Rasad and M. Mohd Yusoff, *Carbohydr. Polym.* 114 (2014) 238.
 33. P. Li, L. Zhao, P. Wei, S. Li, H. Qu, J. Lee, Y. Kong and H. Sun, *Chem. Eng. J.* 231 (2013) 255.
 34. X. Tu, Y. Zhou and Y. Song, *Appl. Surf. Sci.* 400 (2017) 329.
 35. Y.-F. Wu, Y.-N. Liu, S.-W. Guo, S.-N. Zhang, T.-N. Lu, Z.-M. Yu, C.-S. Li and Z.-P. Xi, *J. Power Sources* 256 (2014) 336.
 36. C.M. Burba and R. Frech, *J. Electrochem. Soc.* 151 (2004) A1032.
 37. A. Sadezky, H. Muckenhuber, H. Grothe, R. Niessner and U. Pöschl, *Carbon* 43 (2005) 1731.
 38. F. Pan, W.-l. Wang, D. Chen and W. Yan, *J. Mater. Chem.* 21 (2011) 14680.
 39. A. Jafari, S. Farjami Shayesteh, M. Salouti and K. Boustani, *J. Magn. Magn. Mater.* 379 (2015) 305.
 40. K.S.W. Sing, D.H. Everett, R.A.W. Haul, L. Moscou, R.A. Pierotti, J. Rouquérol and T. Siemieniewska, *Pure Appl. Chem.* 87 (1985) 603.
 41. G. Zhou, D.-W. Wang, F. Li, L. Zhang, N. Li, Z.-S. Wu, L. Wen, G.Q. Lu and H.-M. Cheng, *Chem. Mater.* 22 (2010) 5306.
 42. M. Liu, M. Shi, W. Lu, D. Zhu, L. Li and L. Gan, *Chem. Eng. J.* 313 (2017) 518

© 2018 The Authors. Published by ESG (www.electrochemsci.org). This article is an open access article distributed under the terms and conditions of the Creative Commons Attribution license (<http://creativecommons.org/licenses/by/4.0/>).